# Automated Nuclear Lamina Network Recognition and Quantitative Analysis in Structured Illumination Super-Resolution Microscope Images Using a Gaussian Mixture Model and Morphological Processing

**Yiwei Chen [1], Zhenglong Sun [1], Yi He [1], Xin Zhang [1], Jing Wang [1,2], Wanyue Li [1,2], Lina Xing [1], Feng Gao [1] and Guohua Shi [1,2,3,*]**

[1] Jiangsu Key Laboratory of Medical Optics, Suzhou Institute of Biomedical Engineering and Technology, Chinese Academy of Sciences, Suzhou 215163, China; yiwei.chen@sibet.ac.cn (Y.C.); sunzhl@sibet.ac.cn (Z.S.); heyi@sibet.ac.cn (Y.H.); zhangx@sibet.ac.cn (X.Z.); wj95@mail.ustc.edu.cn (J.W.); lwy321@mail.ustc.edu.cn (W.L.); xingln@sibet.ac.cn (L.X.); gaofeng@sibet.ac.cn (F.G.)

[2] Department of Biomedical Engineering, University of Science and Technology of China, Hefei 230041, China

[3] Center for Excellence in Brain Science and Intelligence Technology, Chinese Academy of Sciences, Shanghai 200031, China

* Correspondence: shigh@sibet.ac.cn

**Abstract:** Studying the architecture of nuclear lamina networks is significantly important in biomedicine owing not only to their influence on the genome, but also because they are associated with several diseases. To save labor and time, an automated method for nuclear lamina network recognition and quantitative analysis is proposed for use with lattice structured illumination super-resolution microscope images in this study. This method is based on a Gaussian mixture model and morphological processing. It includes steps for target region generation, bias field correction, image segmentation, network connection, meshwork generation, and meshwork analysis. The effectiveness of the proposed method was confirmed by recognizing and quantitatively analyzing nuclear lamina networks in five images that are presented to show the method's performance. The experimental results show that our algorithm achieved high accuracy in nuclear lamina network recognition and quantitative analysis, and the median face areas size of lamina networks from U2OS osteosarcoma cells are 0.3184 $\mu m^2$.

## 1. Introduction

The nuclear lamina, which only has a thickness of ~14 nm [1,2], is a complex protein network that organizes major nuclear structures [3–5], and is composed of nuclear lamins [6]. The architectures of nuclear lamina networks are significantly important to biomedicine because of their influence on the genome, and they are also associated with several diseases [7]. More detailed information about the importance of understanding nuclear lamina network structure is written in Appendix A. The architecture of a nuclear lamina network can be imaged by taking advantage of the advances in super-resolution light microscopy [7–13]. One popular tool used for this microscopy is the structured illumination super-resolution microscope [7,13–15]. After acquiring the structured illumination super-resolution microscope images of a nuclear lamina network, nuclear lamina network recognition and quantitative analysis are required to obtain quantitative information on the architecture of the

network [7,13]. Although this can be performed manually, considerable labor and time is required, and the process is also subjective and inaccurate due to the discontinuity of the network in the image. Therefore, several studies have attempted to develop computer vision methods for nuclear lamina network recognition and quantitative analysis [7,13]. The mainstream computer vision method for achieving this goal is based on steerable filters and graph theory [7]. Current available methods can recognize and quantitatively analyze nuclear lamina networks without great errors; however, the results are not very accurate by the judgement of human vision. Thus, it is necessary to design an effective algorithm for nuclear lamina network recognition and quantitative analysis. One efficient method is to use existing high-accuracy image processing methods or their combinations that have not yet been applied in the domain of the nuclear lamina network recognition and quantitative analysis.

Herein, we propose, to the best of our knowledge, the first nuclear lamina network recognition and quantitative analysis algorithm using a Gaussian mixture model (GMM) [16], which is the most common image segmentation algorithm based on finite mixture models [17–19], and morphological processing [20–23]. To confirm the effectiveness of our proposed method, it was used to process five nuclear lamina networks, all of which yielded successful results. The results are presented in this paper.

## 2. Methods

This section describes our automated image processing procedure for nuclear lamina network recognition and quantitative analysis. A flowchart illustrating the proposed algorithm is shown in Figure 1. It includes five steps: pre-processing, image segmentation, network connection, meshwork generation, and meshwork analysis. First, the target region, which contains the lamina, is generated, and bias field correction is applied to this region. Second, the lamina network is segmented via GMM segmentation. Third, network connection is performed by using the morphological closing operation. Fourth, the meshwork is generated by morphological-dilation-based processing. Finally, the geometrical parameters of the meshwork are calculated.
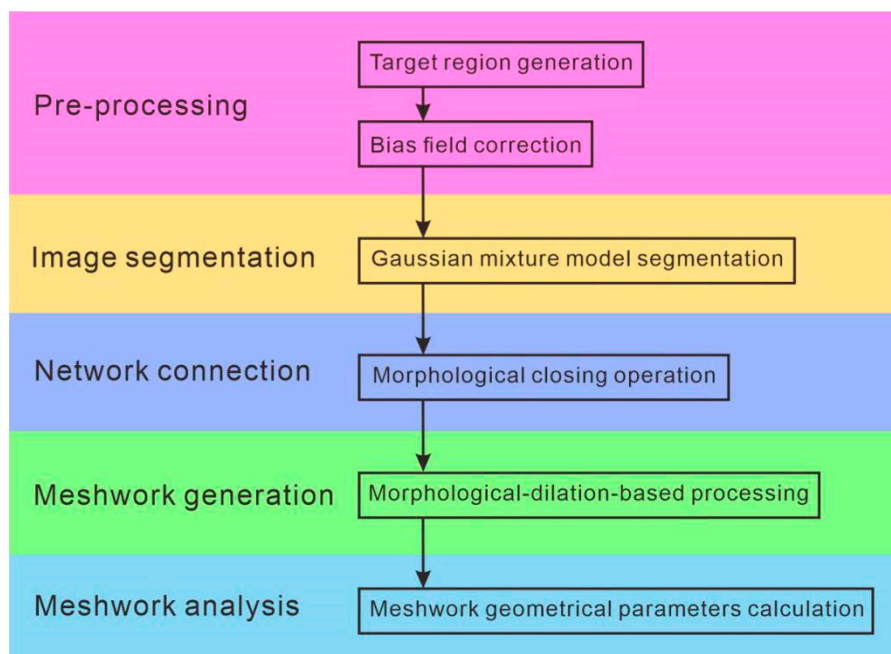


**Figure 1.** Flowchart depicting the image processing steps.

### 2.1. Preprocessing

### 2.1.1. Target Region Generation

To facilitate further image processing, we identified the nuclear lamina region as the target region. First, we segmented the original image with a threshold. Second, we applied the morphological closing and opening operations sequentially to the threshold-segmented image by using OpenCV's morphologyEx function in Python. With these morphological closing and opening operations, we filled small holes and removed small objects from the segmented image. Third, we filled all holes inside the segmented regions to eliminate any residual holes in the segmented regions. Finally, the largest connected region was identified as the target region. An example of target region generation on a representative image, performed using this method, is shown in Figure 2. As shown in the figure, the nuclear lamina region was successfully identified.
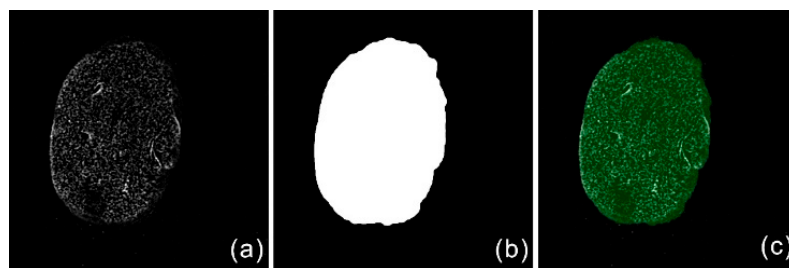


**Figure 2.** Example of target region generation: (**a**) original image, (**b**) generated target region, and (**c**) original image overlaid by target region (translucent green).
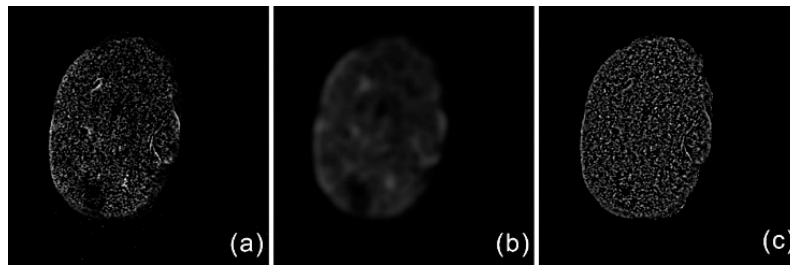
### 2.1.2. Bias Field Correction

To obtain high accuracy segmentation results in the next step, we corrected the image intensity non-uniformity of the nuclear lamina network by using the bias field correction algorithm [24]. An intensity bias field image was created by applying a Gaussian filter with 15-pixels length standard deviation to original image:

$$Bias\ field\ image\ =\ Gaussian\ filter(Original\ image) \tag{1}$$

The original image was corrected by dividing the bias field image within the target region generated in the previous step:

$$Bias\ field\ corrected\ image(x,y)\ = \\ \begin{cases} \underset{Target\ region}{Mean}(Bias\ field\ image) \times \frac{Original\ image(x,y)}{Bias\ field\ image(x,y)} & if\ x,y \in Target\ region \\ \qquad\qquad 0 & if\ x,y \notin Target\ region \end{cases} \tag{2}$$

An example of bias field correction on a representative image, performed using this method, is shown in Figure 3. As shown in the figure, the intensity of the nuclear lamina network image is much more uniform after bias field correction.
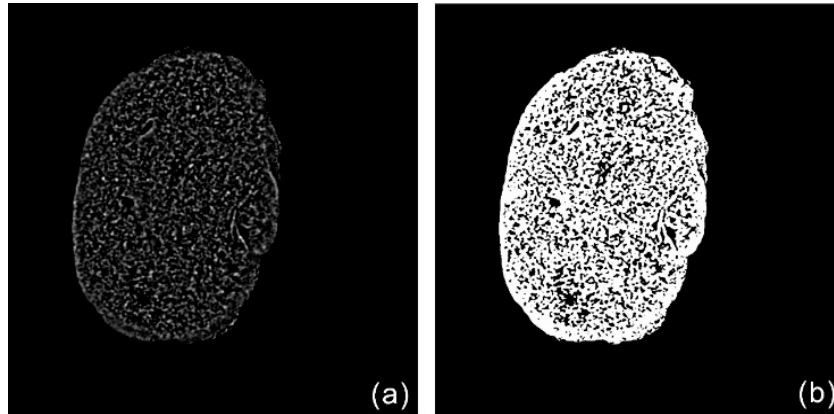
**Figure 3.** Example of bias field correction: (**a**) original image, (**b**) bias field image, and (**c**) bias field corrected image.

## 2.2. Image Segmentation

After preprocessing, we segmented the bias field-corrected image to obtain a rough nuclear lamina network structure using a GMM segmentation algorithm [16]. First, we resized the bias field-corrected image to 30% height and width using OpenCV's resize function in Python to save the computational time. Second, we applied the GMM algorithm to the resized image with two mixture components and five iterations, which provide lowest computation time and acceptable segmentation accuracy. Third, we selected the minimum mean value $\mu$ and the corresponding standard deviation $\sigma$. Finally, we segmented the bias field-corrected image using the following threshold:

$$Threshold = (\mu - 10 \times \sigma) \times 255 \tag{3}$$

An example of image segmentation on a representative image, performed using this method, is shown in Figure 4. As shown in the figure, the nuclear lamina network structure is well segmented.



**Figure 4.** Example of image segmentation: (**a**) bias field corrected image, and (**b**) segmented image.

## 2.3. Network Connection

To close the gaps in the nuclear lamina network structure in the segmented image, we applied network connection to the segmented image. This was implemented by applying the morphological closing operation to the segmented image by using OpenCV's morphologyEx function in Python. An example of network connection on a representative image patch performed using this method is shown in Figure 5. As shown in the figure, the nuclear lamina network structure in the segmented image is well connected after network connection.

**Figure 5.** Example of network connection using the morphological closing operation: (**a**) image before network connection, and (**b**) image after network connection (the network is shown in white and the background is shown in black).

### 2.4. Meshwork Generation

After network connection, we generated the meshwork of the network. First, we generated an initial marked image by setting the foreground of the network-connected image to zero, and we assigned a unique number to each independent connected region in the background of the network-connected image. Second, we iteratively applied the morphological dilation operation to the marked image by using OpenCV's morphologyEx function in Python. This morphological dilation operation dilates the marked image by one pixel from the edge in each iteration. The meshwork is generated where the marked regions connect. After that, dilation is no longer performed on the marked image in locations where the meshwork has been generated. The process of morphological dilation iteration stopped when the marked image was filled with dilated regions. An example of meshwork generation on a representative image patch, performed using this method, is shown in Figure 6. As shown in the figure, the marked regions are gradually enlarged, and meshwork is generated.
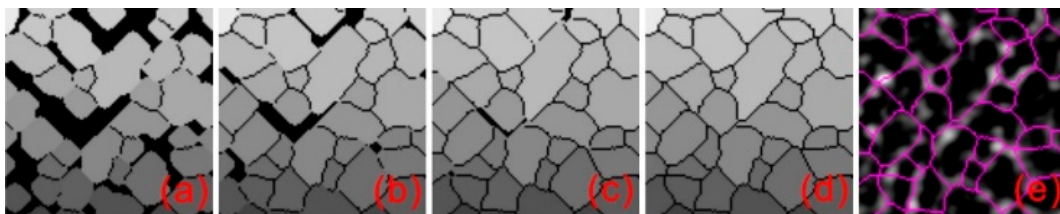


**Figure 6.** Example of meshwork generation: (**a**–**d**) marked images in the morphological dilation iteration process, and (**e**) bias field-corrected image overlaid by meshwork (magenta).

### 2.5. Meshwork Geometrical Parameters Calculation

After meshwork generation, we calculated the meshwork geometrical parameters, defined in [13], considering the junctions, edges, and faces. The faces are determined by the results of the morphological dilation during meshwork generation. The junction pixels must satisfy two conditions: first, the pixels should be located on the meshwork; second, there should be at least three different faces around the pixels. The edges were created because of meshwork segmentation by junctions. An example of junction-marking results on a representative image patch, performed using this method, is shown in Figure 7. As shown in the figure, the junctions were successfully determined. After determining faces, junctions, and edges, we calculated their geometrical parameters by using a pixel-counting method.
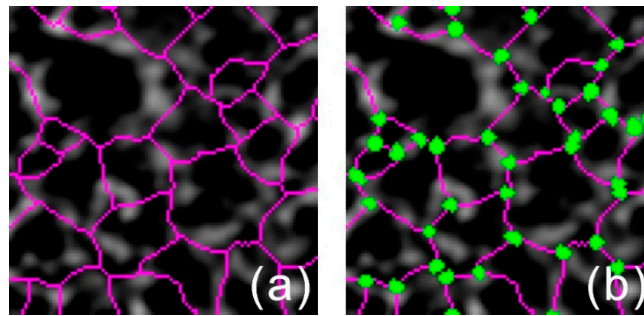
**Figure 7.** Example of junction-marking result: (**a**) recognition image patch, and (**b**) image marked with junctions (green).

## 3. Results

The U2OS osteosarcoma cell line was purchased by the Stem Cell Bank, Chinese Academy of Sciences. The U2OS cells were cultivated in McCoy's 5A medium modified (Thermo Fisher; USA) supplemented with 1% penicillin G and streptomycin (Shenggong; China) as well as 10% fetal bovine serum (Thermo Fisher; Australia) at 37 °C in a 5% (v/v) $CO_2$ environment. Cells were fixed with 4% paraformaldehyde. After blocking in blocking buffer (containing 5% bovine serum albumin, 0.1% Triton X-100 in PBS) for 30min at room temperature, the slides were incubated with primary antibodies against lamin A (1:100, Abcam), then with anti-rabbit IgG conjugated with Alexa Fluor 488 (1:2000, Abcam). Finally, nuclear lamin A network, which is used for our nuclear lamina network recognition and quantitative analysis, were viewed under a ZEISS Elyra 7 (Germany) with Lattice SIM superhigh resolution microscope [25] equipped with alpha Plan-APO 100x/1.46 Oil DIC VIS objective lens.

The typical computational times for processing an image of $1024 \times 1024$ pixels using our automated approach are as follows: 0.209 s for target region generation, 0.101 s for bias field correction, 80.0 s for image segmentation, 0.0105 s for network connection, 12.4 s for meshwork generation, and 22.3 s for meshwork analysis. These computational times were obtained using a system with an Intel Core i5-9400 CPU operating at 2.90 GHz, an NVIDIA GeForce GTX 1660 Ti graphics card, and 16.0 GB RAM. The image denoising program was written in MATLAB (64-bit) and CUDA 10.0, while the other programs were written in Python (64-bit).

To confirm the effectiveness of our method, images from five nuclear lamina networks were obtained. Our method successfully recognized and quantitatively analyzed these nuclear lamina networks in the five datasets. The recognition results are shown in Figure 8. Based on the performance results, it is clear that our algorithm achieves high recognition accuracy with these five samples according to visual inspection by human. Further, the quantitative analysis of faces areas size of these five samples are shown in Figure 9. The median face areas of these five samples ranged from 0.2627 to 0.4248 $\mu m^2$, and the median face areas of all these five samples is 0.3184 $\mu m^2$, which has the same magnitude of order with other research [26] that used different kind of cells.
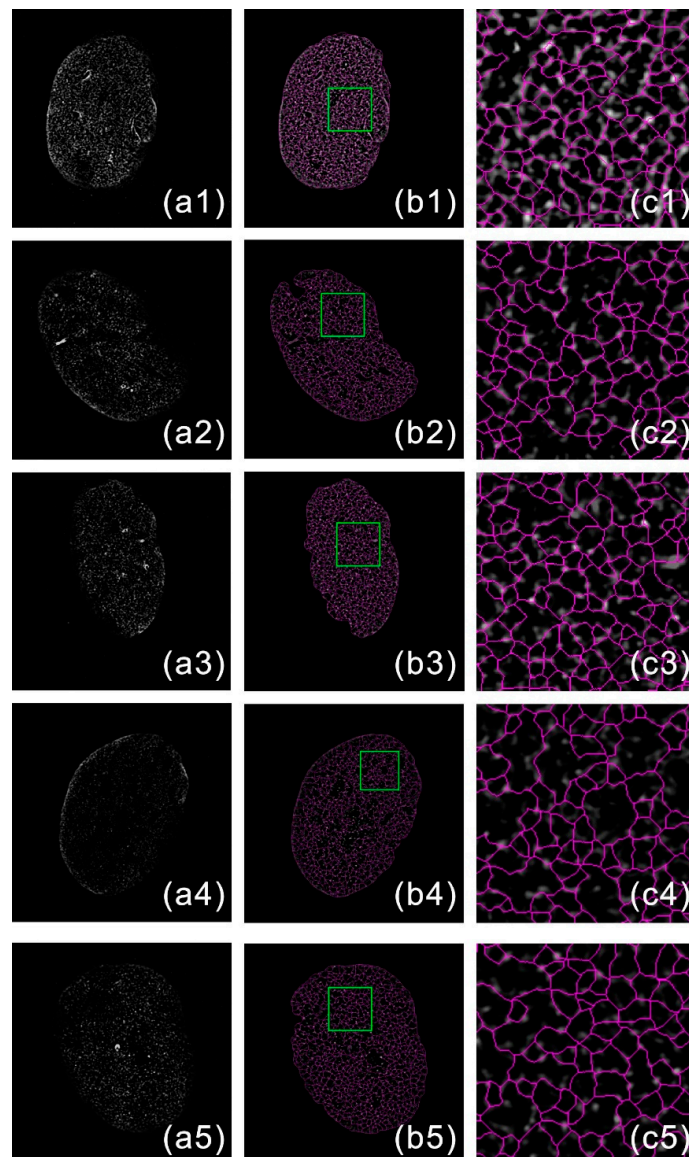
**Figure 8.** Five recognition and quantitative analysis results obtained using the proposed method. (**a**) Input nuclear lamina networks images. (**b**) Recognition images. (**c**) Magnified recognition images.
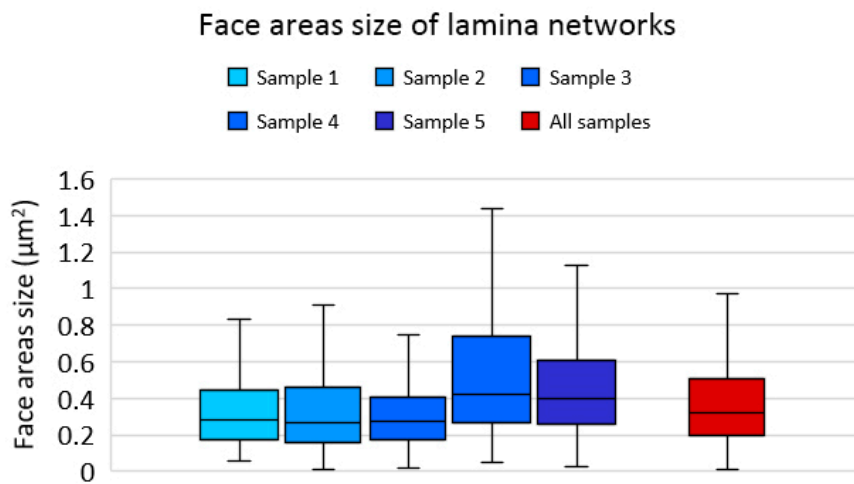


**Figure 9.** Box-plot of face areas from five lamina networks shown in Figure 8.

## 4. Discussion

As mentioned earlier, one efficient method for nuclear lamina recognition and quantitative analysis is to use existing high-accuracy image processing methods or their combinations that have not yet been applied in this domain. Thus, we presented modified versions of three popular methods [27–29] as promising solutions for performing nuclear lamina network recognition and quantitative analysis.

## 5. Conclusions

In this study, an automated method for nuclear lamina network recognition and quantitative analysis was proposed. A GMM and morphological processing were the primary approaches used in our method for analyzing lattice structured illumination super-resolution microscope images. The effectiveness of our approach was confirmed based on the results of target region generation, bias field correction, image segmentation, network connection, meshwork generation, and meshwork analysis. Further, the performance of our method was empirically tested by recognizing and quantitatively analyzing nuclear lamina networks in five images that are presented. The experimental results show that our algorithm can achieve high accuracy in nuclear lamina network recognition and quantitative analysis, and the median face areas size of lamina networks from U2OS osteosarcoma cells are 0.3184 $\mu m^2$, which has the same magnitude of order with other research [26] that used different kind of cells. Our proposed method would be helpful for standard nuclear lamina network recognition and quantitative analysis.

**Conflicts of Interest:** The authors declare no conflict of interest.

## Appendix A. The Importance of Understanding Nuclear Lamina Network Structure

The nuclear lamina is a fibrous structure located beneath the inner nuclear membrane that interacts with chromatin, the nuclear pore complex (NPC), contributing to nuclear structural stability and regulation of chromatin organization in higher eukaryotes [30]. The lamina is primarily composed of two types of lamins: A-type and B-type [31]. Mutations in the *LMNA* gene play a key role in the pathogenesis of a group of diseases called laminopathies. To date, there are approximately 124 mutations in LMNA that cause laminopathies, corresponding to six disease categories: Emery–Dreifuss muscular dystrophy (EDMD), dilated cardiomyopathy (DCM), familial partial lipodystrophy (FPLD), mandibuloacral dysplasia (MAD), autosomal recessive Charcot–Marie–Tooth disorder type 2 (AR-CMT2), and limb girdle muscular dystrophy 1B (LGMD-1B) [32,33]. Mice with the *LMNA* gene knockout exhibit signs of muscular dystrophy, including an abnormal gait, weak forelimbs, and a loss of skeletal muscle mass soon after birth [34]. Cultured *LMNA* knockout cells show abnormal nuclear shapes [35]. Researching the structure of the nuclear lamina composed of lamin A is crucial for understanding laminopathies.

## References

1. Turgay, Y.; Eibauer, M.; Goldman, A.E.; Shimi, T.; Khayat, M.; Ben-Harush, K.; Dubrovsky-Gaupp, A.; Sapra, K.T.; Goldman, R.D.; Medalia, O. The Molecular Architecture of Lamins in Somatic Cells. *Nature* **2017**, *543*, 261–264. [CrossRef] [PubMed]
2. Turgay, Y.; Medalia, O. The Structure of Lamin Filaments in Somatic Cells as Revealed by Cryo-Electron Tomography. *Nucleus* **2017**, *8*, 475–481. [CrossRef] [PubMed]
3. Dechat, T.; Adam, S.A.; Taimen, P.; Shimi, T.; Goldman, R.D. Nuclear Lamins. *Cold Spring Harb. Perspect. Biol.* **2010**, *2*, a000547. [CrossRef]
4. Fawcett, D.W. On the Occurrence of a Fibrous Lamina on the Inner Aspect of the Nuclear Envelope in Certain Cells of Vertebrates. *Am. J. Anat.* **1966**, *119*, 129–145. [CrossRef] [PubMed]
5. Aaronson, R.P.; Blobel, G. Isolation of Nuclear Pore Complexes in Association with a Lamina. *Proc. Natl. Acad. Sci. USA* **1975**, *72*, 1007–1011. [CrossRef]
6. Stuurman, N.; Heins, S.; Aebi, U. Nuclear Lamins: Their Structure, Assembly, and Interactions. *J. Struct. Biol.* **1998**, *122*, 42–66. [CrossRef] [PubMed]
7. Kittisopikul, M.; Virtanen, L.; Taimen, P.; Goldman, R.D. Quantitative Analysis of Nuclear Lamins Imaged by Super-Resolution Light Microscopy. *Cells* **2019**, *8*, 361. [CrossRef]
8. Gustafsson, M.G. Nonlinear Structured-Illumination Microscopy: Wide-Field Fluorescence Imaging with Theoretically Unlimited Resolution. *Proc. Natl. Acad. Sci. USA* **2005**, *102*, 13081–13086. [CrossRef]
9. Hell, S.W.; Wichmann, J. Breaking the Diffraction Resolution Limit by Stimulated Emission: Stimulated-Emission-Depletion Fluorescence Microscopy. *Opt. Lett.* **1994**, *19*, 780–782. [CrossRef]
10. Betzig, E.; Patterson, G.H.; Sougrat, R.; Lindwasser, O.W.; Olenych, S.; Bonifacino, J.S.; Davidson, M.W.; Lippincott-Schwartz, J.; Hess, H.F. Imaging Intracellular Fluorescent Proteins at Nanometer Resolution. *Science* **2006**, *313*, 1642–1645. [CrossRef]
11. Rust, M.J.; Bates, M.; Zhuang, X. Sub-Diffraction-Limit Imaging by Stochastic Optical Reconstruction Microscopy (STORM). *Nat. Methods* **2006**, *3*, 793–795. [CrossRef] [PubMed]
12. Hess, S.T.; Girirajan, T.P.K.; Mason, M.D. Ultra-High Resolution Imaging by Fluorescence Photoactivation Localization Microscopy. *Biophys. J.* **2006**, *91*, 4258–4272. [CrossRef] [PubMed]
13. Shimi, T.; Kittisopikul, M.; Tran, J.; Goldman, A.E.; Adam, S.A.; Zheng, Y.; Jaqaman, K.; Goldman, R.D. Structural Organization of Nuclear Lamins A, C, B1, and B2 Revealed by Superresolution Microscopy. *Mol. Biol. Cell* **2015**, *26*, 4075–4086. [CrossRef] [PubMed]
14. Kner, P.; Chhun, B.B.; Griffis, E.R.; Winoto, L.; Gustafsson, M.G. Super-Resolution Video Microscopy of Live Cells by Structured Illumination. *Nat. Methods* **2009**, *6*, 339–342. [CrossRef] [PubMed]
15. Shao, L.; Kner, P.; Rego, E.H.; Gustafsson, M.G. Super-Resolution 3D Microscopy of Live Whole Cells Using Structured Illumination. *Nat. Methods* **2011**, *8*, 1044–1046. [CrossRef]
16. Reynolds, D.A. Gaussian Mixture Models. In *Encyclopedia of Biometrics*; Springer: Berlin/Heidelberg, Germany, 2009; Volume 741.
17. Bishop, C.M. *Pattern Recognition and Machine Learning*; Springer: Berlin/Heidelberg, Germany, 2006.
18. Bouguila, N. Count Data Modeling and Classification Using Finite Mixtures of Distributions. *IEEE Trans. Neural Netw.* **2011**, *22*, 186–198. [CrossRef]
19. Yuksel, S.E.; Wilson, J.N.; Gader, P.D. Twenty Years of Mixture of Experts. *IEEE Trans. Neural Netw. Learn. Syst.* **2012**, *23*, 1177–1193. [CrossRef]
20. Vincent, L. Morphological Area Openings and Closings for Grey-Scale Images. In *Shape in Picture*; Springer: Berlin/Heidelberg, Germany, 1994; pp. 197–208.
21. Vincent, L. Grayscale Area Openings and Closings, Their Efficient Implementation and Applications. In Proceedings of the EURASIP First Workshop on Mathematical Morphology and Its Applications to Signal Processing, Barcelona, Spain, 10–14 May 1993; pp. 22–27.
22. Tambe, S.B.; Kulhare, D.; Nirmal, M.D.; Prajapati, G. Image Processing (IP) through Erosion and Dilation Methods. *Int. J. Emerg. Technol. Adv. Eng.* **2013**, *3*, 285–289.
23. Jackway, P.T.; Deriche, M. Scale-Space Properties of the Multiscale Morphological Dilation-Erosion. *IEEE Trans. Pattern Anal. Mach. Intell.* **1996**, *18*, 38–51. [CrossRef]

24.　Zang, P.; Liu, G.; Zhang, M.; Dongye, C.; Wang, J.; Pechauer, A.D.; Hwang, T.S.; Wilson, D.J.; Huang, D.; Li, D.; et al. Automated Motion Correction Using Parallel-Strip Registration for Wide-Field En Face OCT Angiogram. *Biomed. Opt. Express* **2016**, *7*, 2823–2836. [CrossRef]

25.　ZEISS Elyra 7 with Lattice SIM: Your Flexible Platform for Fast and Gentle. Superresolution Microscopy. Available online: https://www.zeiss.com/microscopy/int/cmp/lsc/2019/superresolution/elyra-7.html?utm_source=google&utm_medium=cpc&utm_campaign=new-chapter&gclid=EAIaIQobChMI6KKDjeSc7QIVkzArCh34uQ-KEAAYBCAAEgKcxPD_BwE (accessed on 30 November 2020).

26.　Shimi, T.; Pfleghaar, K.; Kojima, S.-I.; Pack, C.-G.; Solovei, I.; Goldman, A.E.; Adam, S.A.; Shumaker, D.K.; Kinjo, M.; Cremer, T.; et al. The A- And B-Type Nuclear Lamin Networks: Microdomains Involved in Chromatin Organization and Transcription. *Genes Dev.* **2008**, *22*, 3409–3421. [CrossRef] [PubMed]

27.　Wen, S.; Liu, W.; Yang, Y.; Huang, T.; Zeng, Z. Generating Realistic Videos from Keyframes with Concatenated GANs. *IEEE Trans. Circuits Syst. Video Technol.* **2019**, *29*, 2337–2348. [CrossRef]

28.　Dong, M.; Wen, S.; Zeng, Z.; Yan, Z.; Huang, T. Sparse Fully Convolutional Network for Face Labeling. *Neurocomputing* **2019**, *331*, 465–472. [CrossRef]

29.　Wen, S.; Dong, M.; Yang, Y.; Zhou, P.; Huang, T.; Chen, Y. End-to-End Detection-Segmentation Network for Face Labeling. *IEEE Trans. Emerg. Top. Comp. Intell.* **2019**, *99*, 1–11.

30.　Moriuchi, T.; Kuroda, M.; Kusumoto, F.; Osumi, T.; Hirose, F. Lamin A Reassembly at the End of Mitosis Is Regulated by Its SUMO-Interacting Motif. *Exp. Cell Res.* **2016**, *342*, 83–94. [CrossRef]

31.　Burla, R.; Carcuro, M.; Torre, M.L.; Fratini, F.; Crescenzi, M.; D'Apice, M.R.; Spitalieri, P.; Raffa, G.D.; Astrologo, L.; Lattanzi, G.; et al. The Telomeric Protein AKTIP Interacts with A- and B-Type Lamines and Is Involved in Regulation of Cellular Senescence. *Open Biol.* **2016**, *6*, 160103. [CrossRef]

32.　Shumaker, D.K.; Kuczmarski, E.R.; Goldman, R.D. The Nucleoskeleton: Lamines and Actin Are Major Players in Essential Nuclear Functions. *Curr. Opin. Cell Biol.* **2003**, *15*, 358–366. [CrossRef]

33.　Perovanovic, J.; Dell'Orso, S.; Gnochi, V.F.; Jaiswal, J.K.; Sartorelli, V.; Vigouroux, C.; Mamchaoui, K.; Mouly, V.; Bonne, G.; Hoffman, E.P. Laminopathies Disrupt Epigenomic Developmental Programs and Cell Fate. *Sci. Transl. Med.* **2016**, *8*, 335ra58. [CrossRef]

34.　Frock, R.L.; Kudlow, B.A.; Evans, A.M.; Jameson, S.A.; Hauschka, S.D.; Kennedy, B.K. Lamin A/C and Emerin Are Critical for Skeletal Muscle Satellite Cell Differentiation. *Genes Dev.* **2006**, *20*, 486–500. [CrossRef]

35.　van Loosdregt, I.A.E.W.; Kamps, M.A.; Oomens, C.W.J.; Loerakker, S.; Broers, J.L.V.; Bouten, C.V.C. Lmna knockout mouse embryonic fibroblasts are less contractile than their wild-type counterparts. *Integr. Biol.* **2017**, *9*, 709–721. [CrossRef]